Energy & Environmental Science

Electronic Structure Basis for Enhanced Overall Water Splitting Photocatalysis with Aluminum Doped $SrTiO_3$ in Natural Sunlight

Journal:	*Energy & Environmental Science*
Manuscript ID	EE-ART-01-2019-000310.R1
Article Type:	Paper
Date Submitted by the Author:	27-Feb-2019
Complete List of Authors:	Zhao, Zeqiong; University of California, Department of Chemistry Goncalves, Renato; University of São Paulo, São Carlos Institute of Physics Barman, Sajib; University of Texas at Arlington, physics Willard, Emma; UC Davis Byle, Edaan; University of California, Davis Perry, Russell; University of California, Davis Wu, Zongkai; University of California, Davis Huda, Muhammad; University of Texas at Arlington, Moule, Adam; UC Davis, Chem Eng and Mat Sci Osterloh, Frank ; University of California, Department of Chemistry

Electronic Structure Basis for Enhanced Overall Water Splitting Photocatalysis with Aluminum Doped $SrTiO_3$ in Natural Sunlight

Zeqiong Zhao,[a] Renato V. Goncalves,[a,b] Sajib K. Barman,[c] Emma J. Willard,[a] Edaan Byle,[a] Russell Perry,[a] Zongkai Wu,[a] Muhammad N. Huda,*[c] Adam J. Moulé,[d] and Frank E. Osterloh*[a]

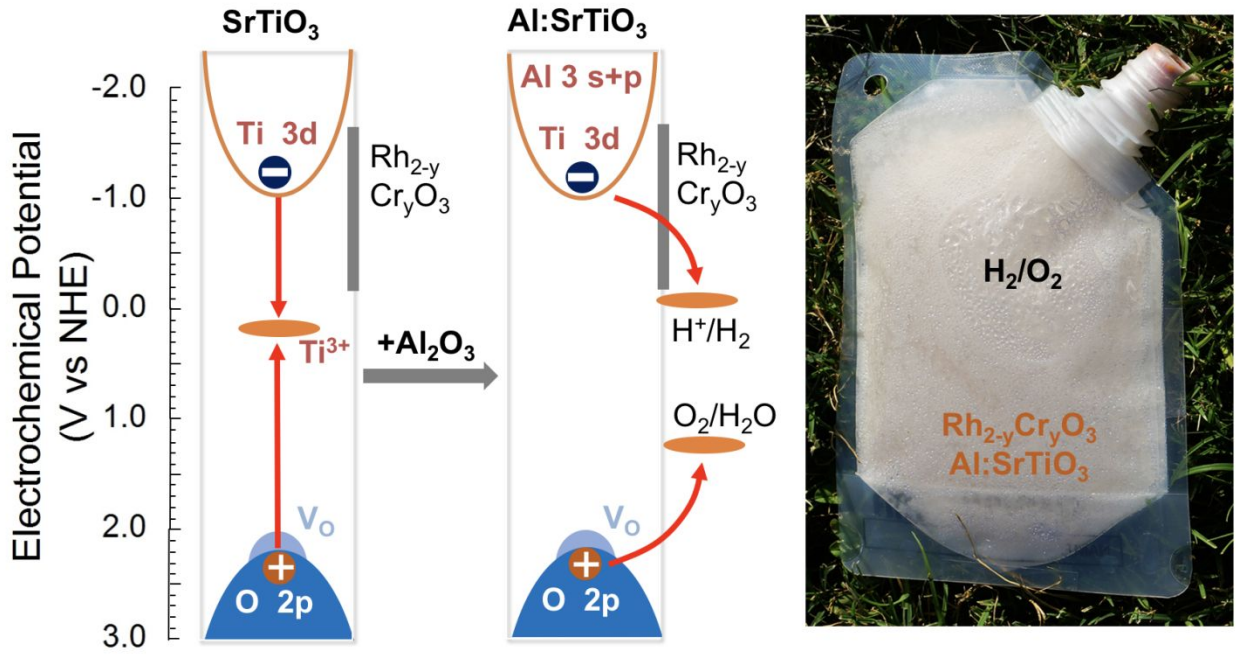

Aliovalently Al^{3+} doped strontium titanate enables overall water splitting in type 1 baggie particle suspension reactor in direct sunlight

ABSTRACT

Overall water splitting with photocatalyst particles presents a potentially cost-effective pathway to hydrogen fuel, however, photocatalysts that can compete with the energy conversion efficiency of photovoltaic and photoelectrochemical cells are still lacking. Recently, Goto et al. reported (*Joule* **2018,** *2* (3), 509-520) that Al-doped $SrTiO_3$ microparticles, followed by modification with Rh_2-

$_yCr_yO_3$ support overall water splitting with 0.4 % solar to hydrogen efficiency and with 56% apparent quantum yield at 365 nm. Earlier, based on transient IR spectroscopy results, the improved activity of Al:$SrTiO_3$ had been attributed to the removal of Ti^{3+} deep recombination sites by the Al^{3+} ions. Here we use X-ray photoelectron spectroscopy to show that Al^{3+} incorporation not only reduces the Ti^{3+} concentration but also diminishes the n-type character of $SrTiO_3$ and shifts the Fermi level to more oxidizing potentials. According to DFT, the electronic structure of Al-doped $SrTiO_3$ depends sensitively on the relative locations of Al^{3+} and oxygen vacancies sites, with Al^{3+} ions next to the oxygen vacancies being most effective at suppressing the Ti^{3+} mid-gap state. Reduced hole and electron trapping resulting from the elimination of Ti^{3+} states is confirmed by surface photovoltage spectroscopy and electrochemical scans. These findings not only provide an experimental basis for the superior water splitting activity of Al-doped $SrTiO_3$, under ultraviolet and solar irradiation, but they also suggest that aliovalent doping may be a general method to improve the solar energy conversion properties of metal oxides. Additionally, overall water splitting with a type 1 single bed particle suspension 'baggie' reactor under direct sunlight illumination with 0.11% solar to hydrogen efficiency is also demonstrated for the first time. This provides a proof of concept for one of the models in the 2009 US Department of Energy Technoeconomic analysis for photoelectrochemical hydrogen production.

INTRODUCTION

As a special form of artificial photosynthesis, overall water splitting (OWS) with powdered photocatalysts is potentially a game changing technology for renewable fuel generation from sunlight. [1, 2] A 2009 Technoeconomic analysis by the US Department of Energy predicts that type 1 single bed particle suspension baggie reactors can produce H_2 at a cost of $1.60/Kg, significantly

below the cost of photoelectrochemical approaches. [2, 3] However, while there are many p-type and n-type semiconductors that promote either H_2 or O_2 evolution from water, only a handful of photocatalysts have been shown to coevolve H_2 and O_2 and without any applied electrochemical and chemical bias.[4-6] Examples of such bias-free OWS photocatalysts include $Rh_{2-y}Cr_yO_3/(Ga_{1-x}Zn_x)(N_{1-x}O_x)$ with an apparent quantum yield (AQY) of 5.9 % at 420-440 nm [7] and the Rh,La:$SrTiO_3$/Mo:$BiVO_4$ tandem in the photocatalyst sheet (1.1% Solar to Hydrogen Efficiency, STH). [8, 9] Long term stability is key to the usefulness of water splitting devices, [10, 11] and therefore the light absorbers must be chosen carefully to avoid photocorrosion. Based on thermodynamics, only metal oxides have intrinsic stability to persist under the corrosive conditions of water electrolysis. However, the large band gap of metal oxide OWS photocatalysts, such as La-doped $NaTaO_3$ (E_G = 4.1 eV, AQY=56% at 270 nm) [12] and Zn-doped Ga_2O_3 (E_G = 4.4 eV) [13] precludes sunlight driven OWS. [4, 14, 15] $SrTiO_3$ has continued to draw interest as OWS photocatalyst because its relatively narrow 3.2 eV bandgap allows for some sunlight absorption, even though quantum efficiencies for H_2 evolution remained low. [16-25] Beginning in 2009, the Domen lab and others [26] reported that doping of $SrTiO_3$ with other mono-, bi- or trivalent main group element cations (M = Li^+, Na^+, K^+, Rb^+, Cs^+, Mg^{2+}, Al^{3+}, Ga^{3+} and In^{3+}) led to significant OWS improvements [27-32] when the absorber was combined with the proton-selective reduction catalyst $Rh_{2-y}Cr_yO_3$. [33, 34] Recently, an AQY of 56% at 360 nm and 0.4% efficient water splitting under sunlight was observed when Al^{3+} was used as a modifier. [31, 35] The activity persisted for over 1,000 h.[36] It has been speculated that the aliovalent dopant suppresses Ti^{3+} states which are involved in electron-hole pair recombination.[27] Indeed, for the Al^{3+} modified material, mid IR transient absorption spectroscopy confirmed extended electron hole carrier lifetimes. [29] However, to date, there is no experimental data available on the effect of Al^{3+} on the electronic band structure of the material.

In order to close this knowledge gap, we perform here experimental and theoretical studies on the electronic structure of Al-doped $SrTiO_3$ and on charge carrier separation in the material. According to X-ray photoelectron spectroscopy (XPS), Al^{3+} incorporation suppresses Ti^{3+} states and shifts the Fermi level away from the conduction band edge. Density Functional Theory (DFT) calculations reveal a sensitive dependence of the electronic structure on the proximity between Al^{3+} and oxygen vacancy sites V_O. Complete elimination of sub-band gap states is observed only when the oxygen vacancies V_O are in the coordination sphere of two Al^{3+} ions. Moving one or both Al^{3+} ions further away from the V_O sites leads to the formation of Ti^{4+} mid gap states near the vacancies. These $\{Ti^{4+}\text{-}V_O\}$ oxygen vacancy complexes remain unoccupied by electrons due to the shift of the Fermi level to more oxidizing potentials. These are responsible, however, for a weak 1.7-3.2 eV feature that is observed in optical absorption spectra of Al-doped $SrTiO_3$. [37] Along with the suppression of the Ti^{3+} states, reduced electron trapping and improved surface photovoltage are observed in electrochemical measurements and surface photovoltage spectra of Al-doped $SrTiO_3$. These findings provide an experimental basis for the superior water splitting activity of Al-doped $SrTiO_3$ under UV and solar irradiation. [31, 35] Overall, this work suggests that aliovalent doping with closed shell metal ions may be a general method to control charge trapping sites in metal oxides and to improve their photocatalytic properties.

Experimental Section

Titanium (IV) oxide P25 (99.5%, Acros Organics), strontium carbonate (99.9%, Aldrich), strontium chloride hexahydrate (99%, EM Science), rhodium chloride (>99%), chromium (III) nitrate nonahydrate (99%, Acros Organics), alumina crucible (Fisher) were used as received. Water was purified to 18 MΩ·cm resistivity by a Nanopure system.

Synthesis of Al:$SrTiO_3$:[31] 3.10 g of $SrCO_3$ was calcined in air at 300 °C for 1 h before use. 1.68 g TiO_2 and 3.10 g $SrCO_3$ were well mixed by wet grinding with a small volume of added ethanol for 3 times. Afterwards, the mixture was heated at 1000 °C for 10 hours in a covered ceramic crucible. 0.37 g obtained $SrTiO_3$ was ground with 5.33 g $SrCl_2 \cdot 6H_2O$ (mole ratio of $SrCl_2/SrTiO_3$ =10) for 5 min. The mixture was then heated at 1100 °C for 10 h in a covered alumina crucible. The resulting Al:$SrTiO_3$ / $SrCl_2$ solid was washed with water until no more white AgCl precipitate formed in rinse solutions upon adding $AgNO_3$. The overall yield for Al:$SrTiO_3$ is >90%, based on TiO_2.

Deposition of $Rh_{2-y}Cr_yO_3$ co-catalyst:[38-40] 150 mg Al:$SrTiO_3$ and 4 mL water containing an appropriate amount of $RhCl_3$ and $Cr(NO_3)_3$ were placed in a vial inside of a water bath at 70 °C and slowly evaporated under constant stirring. The resulting powder was collected and heated in air at 350 °C for 1 h to produce $Rh_{2-y}Cr_yO_3$ loaded Al:$SrTiO_3$ in 95% yield.

Scanning electron microscopy (SEM) and energy dispersive x-ray spectroscopy (EDX) were conducted on Philips XL-30 Scanning Electron Microscope and Scios DualBeam Scanning Electron Microscope. Samples were prepared by drop-coating a few drops of the sample suspension onto a silicon wafer followed by drying in air. Powder X-ray diffraction scans were performed using a Bruker D8 Advance Eco with a Cu Kα X-ray radiation and a monochromatic wavelength of 1.5418 Å. UV/Vis diffuse reflectance spectra and absorption spectra were recorded on a Thermo Scientific Evolution 220 UV Vis spectrometer equipped with an integrating sphere. Surface photovoltage spectroscopy (SPS) measurements were conducted under vacuum (1 x 10^{-4} mBar) using a gold Kelvin probe (Delta PHI Besocke) as the reference electrode. Samples were illuminated with monochromatic light from a 150 W Xe lamp filtered through an Oriel Cornerstone 130 monochromator. The light intensity at the sample was 0.1-0.3 mW cm^{-2}. Spectra were

corrected for drift effects by subtracting a dark scan. Particle films were prepared via the following method. First, fluorine-doped tin oxide (FTO) substrates were sonicated sequentially in methanol, acetone and 2-propanol, rinsed with water, and dried under vacuum before use. Gold substrates were sonicated in acetone, soaked in 30% H_2O_2 and 0.1 M KOH solution for 15 min, and then rinsed with water, and dried under vacuum before use. In general, 6 mg Al:$SrTiO_3$ or $SrTiO_3$ was suspended in 1 mL water and then sonicated for 3 h. Then 0.1 mL Al:$SrTiO_3$ suspension was dropped coated on 0.8 x 0.8 cm^2 substrates, followed by heating at 300 ^oC for 2 h in air. The film thickness was measured with a Dektak 150 profilometer after the SPS measurement.

Chemical surface analysis was performed by X-ray photoelectron spectroscopy (XPS) using a spectrometer (Scienta-Omicron ESCA+) with a high-performance hemispheric analyzer (EAC-2000 sphere) with monochromatic Al Kα source (h ν = 1486.6 eV) radiation as the excitation source. The operating pressure in the ultra-high vacuum chamber (UHV) during the analysis was 10^{-9} Pa. The XPS survey spectra were recorded at constant pass energy of 50 eV with a 0.5 eV per step. The high-resolution core levels and the valence band position spectra were recorded with pass energy of 50 eV with a 0.05 eV per step. To eliminate charging effects, a low energy electron flood gun was used. The positions of the peaks in the spectra were corrected in relation to the binding energy of the carbon peak (C1s) set at 284.8 eV. Peak fitting of the high-resolution spectra were processed using the CasaXPS software (Casa Software Ltd). A Shirley background subtraction was performed before the curve fitting for all data. Valence band XPS data were calibrated by linear extrapolation of the signal to zero intensity and by equating the zero intensity point to 0 eV binding energy, which is the Fermi level of the sample, by definition.

For photoelectrochemical measurements, thin films of $SrTiO_3$ and Al:$SrTiO_3$ microparticles were prepared by drop coating on F:SnO_2 (FTO) substrates and annealing at 500°C

for 2 hours. The working electrode was connected in a 3-electrode configuration with a Pt counter electrode and a saturated calomel reference electrode (SCE). Aqueous electrolyte solution (0.1 M K_2SO_4) were added to the cell and bubbled with N_2 gas to remove all dissolved oxygen prior to scanning. The system was calibrated to vs NHE using the redox potential of $K_4[Fe(CN)_6]$ at +0.358 V vs. NHE.

Photocatalytic hydrogen and oxygen evolution tests were performed by dispersing 100 mg of the catalysts in 100 mL water in a 165 mL quartz glass flask connected directly to a Varian 3800 gas chromatograph with a 60/80 Å molecular sieve column and thermal conductivity detector. The catalyst dispersion was sonicated for 15 min and degassed with N_2 for 20 min to remove the residual oxygen gas dissolved in the water. The flask was then purged with argon and the solution mixture was irradiated with a Xe lamp. The light intensity was measured at the flask surface by an International Light IL1400BL photometer equipped with a GaN detector (SED (SEL) 365 with 230 to 380 nm sensitivity). OWS experiments under direct sunlight illumination were conducted using a polypropylene bag of 169.7 cm^2 surface area mounted on a silver coated metal reflector. The bag was filled with 120 mL of water and 0.300 g of the catalyst powder and then sealed with a septum fitted plastic cap. The bag was laid flat and exposed to direct sunlight for 4 h periods, after which the evolved gases were measured volumetrically via syringe, and the gas composition was determined via gas chromatography analysis. About 35% of the evolved H_2 was lost to diffusion through the plastic walls of the bag. Light intensity measurements (Supporting information) were conducted every hour using an International Light IL1400BL photometer equipped with a GaN detector (SED (SEL) 365 of 230 to 380 nm range), a thermopile (SED 623 of 200 - 4200 nm range), and a GaAsP visible light detector (SED (SEL) 005 of 260-680 nm range).

The theoretical part of this work was carried out within the density functional theory (DFT) framework [41, 42] as implemented in the Vienna ab-initio simulation package.[43, 44] The projected augmented wave (PAW) method [45, 46] was used for better computational efficiency and the calculations were performed in the generalized gradient approximations (GGA) through the Perdew Burke-Ernserhof (PBE) exchange-correlation.[47] For simulations, a 40 atom supercell of $SrTiO_3$ ($2 \times 2 \times 2$) is considered in its perovskite structure, which contains 8 unit cells. The size of the supercell remains the same for all total energy and electronic structure calculations. The oxygen vacancy is generated by removing an O atom from its site and doping is achieved by replacing two Ti atoms with Al atoms. All of the structures used in this work were geometrically optimized without any symmetry constraint before calculating the total energy and electronic structure. The kinetic energy cut-off for the plane wave basis set was 500 eV. For ionic relaxation, the force on each ion was set equal to or less than 0.01 eV/Å. In the electronic self-consistent loop, the allowed error for the global break condition was equal to or less than 1E-06 eV. The Brillouin zone was sampled using a 13 X 13 X 13 *k*-grid generated by the Monkhorst-Pack method [48] for all the supercells. Since GGA underestimates the band gap and since it is well known for transition metals that GGA fails to treat *d* and *f* electrons properly, we have adopted the GGA + U method for the electronic structure calculations. In this study, the GGA + U method was implemented with Dudarev's approach,[49] with U = 7 and J = 1 on the Ti *d* orbital. This choice of U and J values gives an indirect band gap of 3.25 eV and direct band gap of 3.60 eV for pure $SrTiO_3$, in good agreement with the experimental band gaps.

RESULTS AND DISCUSSION

The Al-doped $SrTiO_3$ perovskite was synthesized as described previously by Ham et al. [31] and its structure type and cubic morphology were confirmed by powder x-ray diffraction (PXRD) and scanning electron microscopy (SEM) (**Figure S1**).[37] According to X-ray fluorescence measurements, Al-doped $SrTiO_3$ contains 1.2 atom% of Al. Based on the ion radius (54 pm for hexa-coordinated Al^{3+}), the Al^{3+} ions mostly likely substitute Ti^{4+} ions (61 pm) in the lattice. The active photocatalyst (PC) is obtained after modification of Al-doped $SrTiO_3$ with $Rh_{2-y}Cr_yO_3$ cocatalyst (0.1 wt% Rh and 0.1wt% Cr). [40] According to energy dispersive X-ray spectroscopy (EDX, **Figure 1c**), the co-catalyst is evenly distributed on the Al:$SrTiO_3$ surface.

Figure 1a shows a suspension of the catalyst inside of a polypropylene bag exposed to natural sunlight. Gas bubble formation becomes visible within an hour (a time lapse **video** in supporting information) and continues with rates up to 4 mL per hour. Based on the data in **Figure 1d** and **Table S1**, the solar to hydrogen efficiency under these conditions is estimated as 0.11%. To our best knowledge, this is the first demonstration of sunlight-driven overall water splitting with a type 1 single bed particle suspension baggie reactor. [2, 3] Energy efficiencies of up to 0.4 % STH have been measured for fixed bed configurations (panels or sheets) with the Al:$SrTiO_3$ catalyst. [31, 35, 36] The lower efficiency of the suspension is in part due to the optical shading from the polypropylene bag (**Figure S2c**).

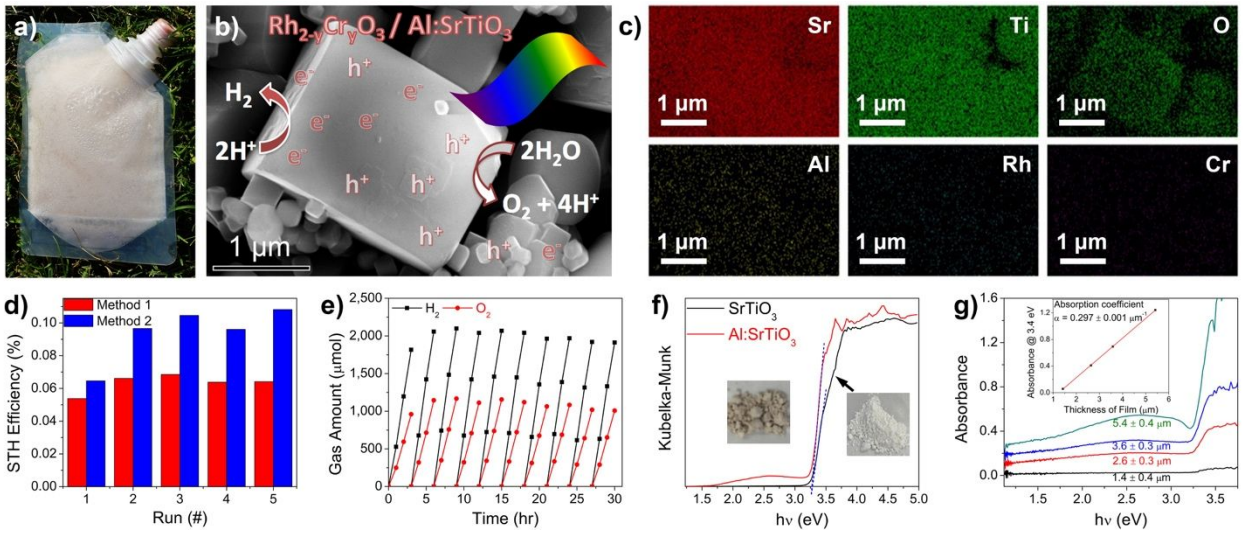

Figure 1. (a) Gas evolution from $Rh_{2-y}Cr_yO_3$ (0.1 wt% Rh, 0.1 wt% Cr)-loaded Al:$SrTiO_3$ photocatalyst (PC) suspension in a polypropylene bag after 4 hour direct sunlight irradiation. (b) SEM and (c) EDX results for the particle shown in (b). (d) Solar to hydrogen efficiencies of suspended PC in bag, computed on the basis of detected H_2 amount (method 1) or detected O_2 amount (method 2). For details see **Figure S2**. (e) H_2/O_2 evolution from 100 mg PC in 100 mL of pure water under Xe lamp irradiation (29 mW/cm^2 by UV detector, 8 cm^2 illumination area). (f) UV-Vis diffuse reflectance spectra and photos of $SrTiO_3$ and Al:$SrTiO_3$. (g) Absorption spectra of flux Al:$SrTiO_3$ films versus thickness. A linear fit at 3.4 eV (insert) establishes the absorption coefficient $\alpha = 0.297\ \mu m^{-1}$ at 3.4 eV.

When the experiments are repeated in a closed loop system under monochromatic illumination at 375 nm, stoichiometric H_2/O_2 evolution is observed with an apparent quantum yield (AQY) of 14.5 % (**Table S1**). Previously, AQY values of 30-56% at 360 nm (3.44 eV) had been reported for the $Rh_{2-y}Cr_yO_3$/Al:$SrTiO_3$ system. [31, 35, 36] A lower AQY at 375 nm (3.31 eV) that is observed here is due to the lower optical absorption at this wavelength (**Figure 1f**). Under full spectrum Xe illumination (**Figure 1e**) the catalyst suspension produces H_2 steadily at a rate of 285

μmol h^{-1} with no decay over 30 hours and a turnover number of 36.5, based on the molar amount of $SrTiO_3$. Under identical conditions, the hydrogen evolution rate of non-Al-modified $Rh_{2-y}Cr_yO_3/SrTiO_3$ is only 1 μmol h^{-1}. This confirms earlier studies that the improved solar energy conversion ability of Al:$SrTiO_3$ is correlated with Al content. [27, 31, 37]

In order to observe the electronic structure changes brought about by introduction of Al lattice, X-ray photoelectron spectra (XPS) were recorded for $SrTiO_3$ and for Al-doped $SrTiO_3$. **Figure 2a** shows the Ti 2p core-level XPS spectrum for non-Al doped $SrTiO_3$ prepared by solid state reaction. The spectrum for $SrTiO_3$ is similar to XPS spectra reported in the literature. [50-52] The doublet at 458.6 and 464.4 eV can be assigned to the Ti $2p_{3/2}$ and Ti $2p_{1/2}$ components of Ti^{4+}. A second doublet at 457.2 and 463.1 eV reveals the presence of Ti^{3+} species in the material. [53] Based on the relative peak ratios, 72.8 % of titanium is present as Ti^{4+} and 27.2% as Ti^{3+}. The latter are believed to be mostly at the surface of the particles, as samples of $SrTiO_3$ with high Ti^{3+} lattice concentration are intensively colored while the $SrTiO_3$ particles here appear white. [52] In contrast, the XPS spectrum for Al-doped $SrTiO_3$ (**Figure 2b**) only shows one single spin-orbital doublet feature of Ti^{4+} but no discernable contribution of Ti^{3+}. This confirms that the introduction of Al^{3+} ions prevents the formation of Ti^{3+} ions in the lattice of $SrTiO_3$, as hypothesized by Takata et al.[27] Additionally, incorporation of Al^{3+} ions is found to also modify the high-resolution O 1s region of $SrTiO_3$ as shown in **Figures 2 (c)** and **(d)**. The main peak at 529.8 can be assigned to O^{2-} ions in the lattice, whereas the peak at 531.9 eV has been previously assigned to hydroxyl-groups at the particle surfaces.[54-56] The small peak at 528.6 eV is tentatively attributed to lattice O^{2-} ions bonded to Ti^{3+} ions in the lattice. This interpretation is supported by the disappearance of the 528.6 eV peak for Al-doped $SrTiO_3$ in **Figure 2 (d)**, which no longer contains any Ti^{3+}. At the same time, the 531.3 eV peak belonging to surface hydroxyl groups is increased to 32 % and the 529.2 eV of

the lattice O^{2-} ions is decreased to 56 %. This suggests an increase of the surface concentration of hydroxyl groups in Al-doped $SrTiO_3$. To test this assumption, infra-red (IR) absorption spectra were recorded for both compounds (**Figure S4).** The spectrum of $SrTiO_3$ does indeed show O-H stretching vibrations from the presence of surface adsorbed water or hydroxyl groups, however, these bands no longer exist in the vibrational spectra of Al-doped $SrTiO_3$. This means that the increased 531.3 eV signal must be due to other species. Tentatively, we attribute it to the O^{2-} ions bonded to Al^{3+} ions near the surface. This is supported by XPS studies on Al_2O_3, which show the O 1s peak at 531.8 eV.[57] The XPS O1s core spectrum of Al-doped $SrTiO_3$ also contains a new peak at 533.1 eV (12% of the total) that is attributed to $SrCO_3$ species, that are produced as a side product during the $SrCl_2$ flux treatment. [54, 58]

Detailed inspection of the Ti and O core level spectra also reveals a general 0.5-0.6 eV shift of all peaks to lower binding energy. This global shift can be attributed to a change in the charge distribution of the sample, as brought about by a change of the depletion layer. [59, 60] Depletion layers in $SrTiO_3$ and Al:$SrTiO_3$ form when the Fermi level of the metal oxide equilibrates with that of the XPS sample holder. [61] The direction of the signal shift to lower binding energy in Al-doped $SrTiO_3$ indicates that the Fermi level in Al:$SrTiO_3$ is more oxidizing than in non-doped $SrTiO_3$. As a result, Al:$SrTiO_3$ is less depleted of electron majority carriers, which agrees with the lower concentration of Ti^{3+} states in Al:$SrTiO_3$. Analogously, chemically reduced $SrTiO_3$ samples with higher Ti^{3+} content and more reducing Fermi level produce XPS signal shifts to more oxidizing energy.[52]

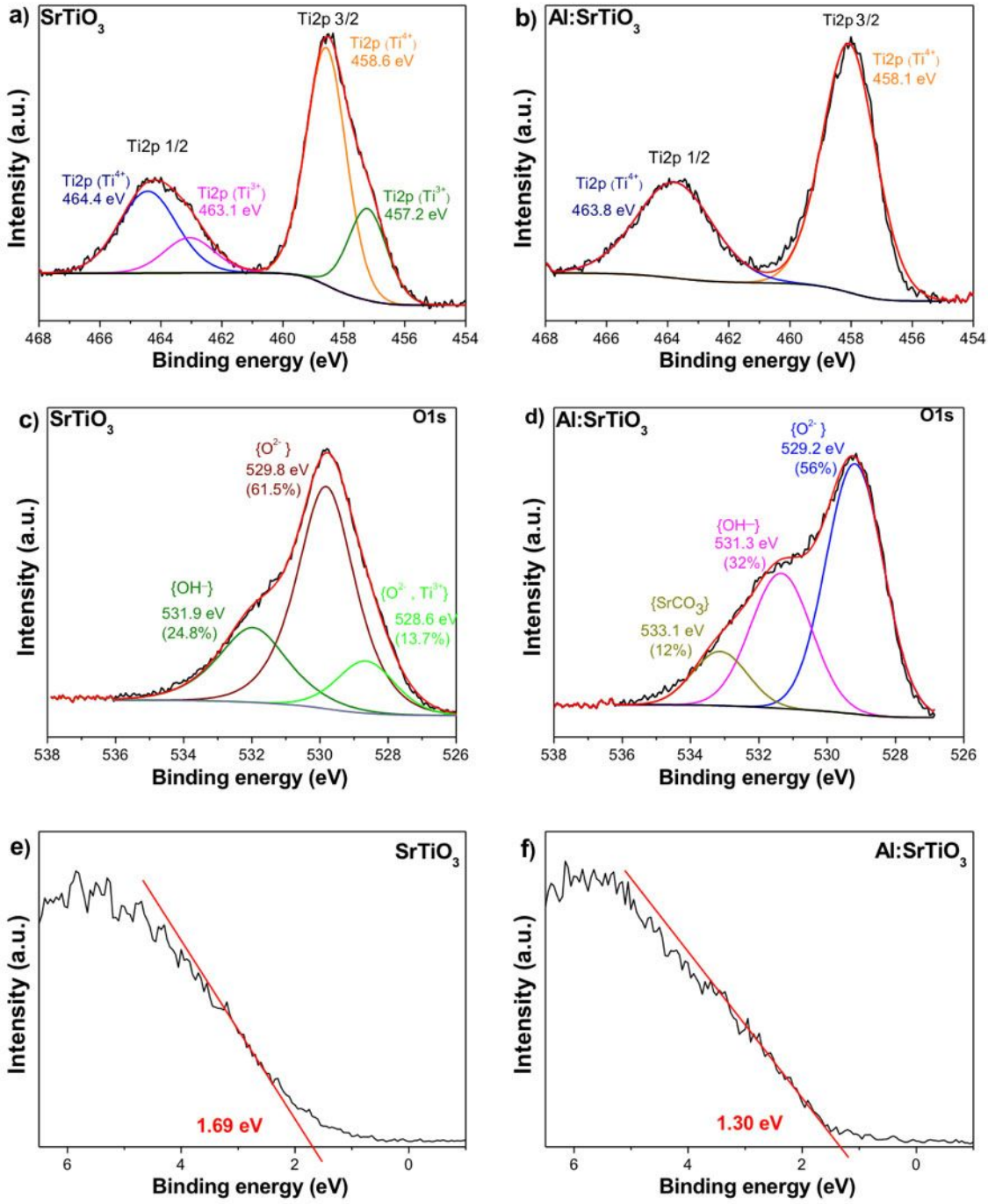

Figure 2. High resolution XPS spectra of Ti 2p region in (a) pure $SrTiO_3$ and (b) Al:$SrTiO_3$ and XPS spectra of O 1s region in (c) pure $SrTiO_3$ and (d) Al:$SrTiO_3$. All O and Ti peaks move 0.5-0.6 eV to lower binding energy in Al:$SrTiO_3$. Valence band edge XPS spectra of (e) pure $SrTiO_3$ and (f) Al:$SrTiO_3$.

Valence band edge XPS spectra for pure and Al-doped $SrTiO_3$ are shown in **Figure 2 (e)** and **(f)**. In both spectra, the peak around 6 eV is due to ionization of valence band states formed by O 2p and Ti 3d orbital hybridization. Pure $SrTiO_3$ has a VB edge energy of 1.69 eV, relative to its Fermi level, estimated by linear extrapolation of the peaks to the baseline. For Al-doped $SrTiO_3$ the VB edge is observed at lower energy (1.30 eV). This 0.39 eV shift in reducing direction corresponds to the shift observed in the Ti and O core level spectra; thus, it is viewed as a result of lower electron depletion in Al-doped $SrTiO_3$, as discussed above.

The observed changes in Ti^{3+} content and upon Al^{3+} doping can be explained on the basis of defect equilibria in $SrTiO_3$ (Equations 1-4) that are expressed using the Kröger-Vink notation. [27, 62, 63] Thermal annealing of non-doped $SrTiO_3$ in air or under vacuum is known to produce oxygen vacancies in the lattice according to Eq. 1. [18, 64, 65] To maintain charge neutrality, the loss of each oxide ion must be accompanied by the formation of two Ti^{3+} ions (Eq.2). This is the reason for the n-type character of $SrTiO_3$ and the blue color of vacuum-annealed $SrTiO_3$. [66] In Al-doped $SrTiO_3$, the Al^{3+} ions can substitute for Ti^{3+}, reducing the concentration of the latter, and resulting in a decrease of the n-type character of the Al-doped $SrTiO_3$. Additionally, Al^{3+} can substitute Ti^{4+} ions in the lattice, leading to the formation of oxygen vacancies, according to Eq. 3. If these formed oxygen vacancies are accompanied by oxygen uptake from the air, according to Eq.4, holes are created and the material becomes p-type.

$$O^x_O \rightarrow V^{\bullet\bullet}_O + \tfrac{1}{2} O_2 + 2\, e^{/} \qquad \text{Eq. 1}$$

$$2e^{/} + 2\, Ti^x_{Ti} \rightarrow 2\, Ti^{/}_{Ti} \qquad \text{Eq. 2}$$

$$Al_2O_3 + 2\ Ti^{x}_{Ti} \rightarrow 2\ Al^{/}_{Ti} + V^{\bullet\bullet}_{O} + 2\ TiO_2 \quad \text{Eq. 3}$$

$$V^{\bullet\bullet}_{O} + \tfrac{1}{2}\ O_2 \rightarrow O^{X}_{O} + 2h^{\bullet} \quad \text{Eq. 4}$$

In order to better understand how the electronic structure of $SrTiO_3$ is modified by Al^{3+} incorporation, DFT calculations were conducted on $SrTiO_3$ in the absence and presence of oxygen vacancies and Al^{3+} dopants. The density of states diagram and band structure of pure, defect free $SrTiO_3$ are shown in **Figure 3a** and in **Figure S5/S6a**. The results match that of earlier calculations. [67-69] The conduction band edge is composed mainly of empty Ti 3d orbitals and the valence band edge mainly consists of filled O 2p states. The generalized gradient approximations (GGA)-calculated indirect bandgap of 1.77 eV and direct band gap of 2.16 eV are below the experimental values, which is a consequence of the known underestimation of the on-site Coulomb interaction for d and f electrons by GGA-DFT. The application of the Hubbard parameter U (U = 7 and J = 1) fixes this problem and leads to value of 3.25 eV for the indirect gap and 3.60 eV for the direct gap, close to the experimental values seen here and in the literature. [17] The band structure changes when a single oxygen vacancy V_O is added to the 40 atom-supercell, as shown in **Figure 3b and S6b**. First, the Fermi level shifts to the conduction band edge, which is due to the creation of two Ti^{3+} ions (see **Eq. 1** and **2**). Second, new Ti^{3+} states form 0.8-1.3 eV below the $SrTiO_3$ conduction band edge. Excitation of these states is responsible for the deep blue/black color of vacuum annealed or reduced $SrTiO_3$,[18] which is associated with a broad optical absorption from 775 nm (1.6 eV) to above 2000 nm (0.62 eV), depending on the presence of other metal impurities. [64, 66] Clearly, the presence of Ti^{3+} states in Al:$SrTiO_3$ can be ruled out on the basis of the combined DFT, XPS and optical absorption data. As **Figure 3c** shows, the Ti^{3+} defect band in $SrTiO_3$ disappears when two Ti^{4+} sites in the super cell containing the oxygen vacancy are replaced with

Al^{3+} ions. Due to the loss of two Ti^{3+} donors, the Fermi level returns to the top of the valence band edge. The added Al^{3+} s and p states are deeply embedded in the conduction band at 0.42 eV above the conduction band edge (**Figure S7**). According to **Figure 3**, the detailed electronic structure of Al-doped $SrTiO_3$ strongly depends on the distance of the Al^{3+} ions from the oxygen vacancy V_O. If both Al^{3+} ions are next to the oxygen vacancy as in **Figure 3c**, the bandgap of Al-doped $SrTiO_3$ resembles that of the undoped, oxygen vacancy-free $SrTiO_3$, except for a lower degeneracy of the bands resulting from the lower symmetry of the cell (**Figure S6c**). As the two Al^{3+} ions are placed farther away from the vacancy, a band gap reduction to 2.5 eV can be observed, which results from lowering the conduction band edge (**Figures 3e** and **S6e**). These new states have mixed contributions from Ti d orbitals and O p orbitals (**Figure S7b**) and belong to the Ti^{4+} and O^{2-} ions next to the oxygen vacancy. The states from these $\{Ti^{4+}\text{-}V_O\}$ vacancy complexes are already observable in the model with only one Al^{3+} near the V_O and one far away from it (**Figure S6d**), even though in that case, the effect on the band gap of the compound is less significant. The more reducing potential of the Ti^{4+} states in comparison to the Ti^{3+} states in Al-free $SrTiO_3$ can be understood on the basis of molecular orbital theory. Because the extra electron in the $\{Ti^{3+}\text{-}V_O\}$ is located in an antibonding Ti d/O p orbital, it weakens the Ti-O bond and moves the antibonding state energy below that for the $\{Ti^{4+}\text{-}V_O\}$ vacancy complex. The new $\{Ti^{4+}\text{-}V_O\}$ states in **Figure 3e** may be responsible for the weak absorption at 1.7-3.2 eV that is seen in the optical spectra (**Figure 1f**) of Al-doped $SrTiO_3$ and which causes the pale-brownish appearance of the material (**Figure 1f insert**). [37] Related states at 1.9-2.6 eV in non-doped $SrTiO_3$ have been previously attributed to a combination of self-trapped excitons, oxygen vacancies and oxygen vacancy complexes in the lattice and at the surface.[66, 70] Similar states are also seen in the photoluminescence of TiO_2.[71]

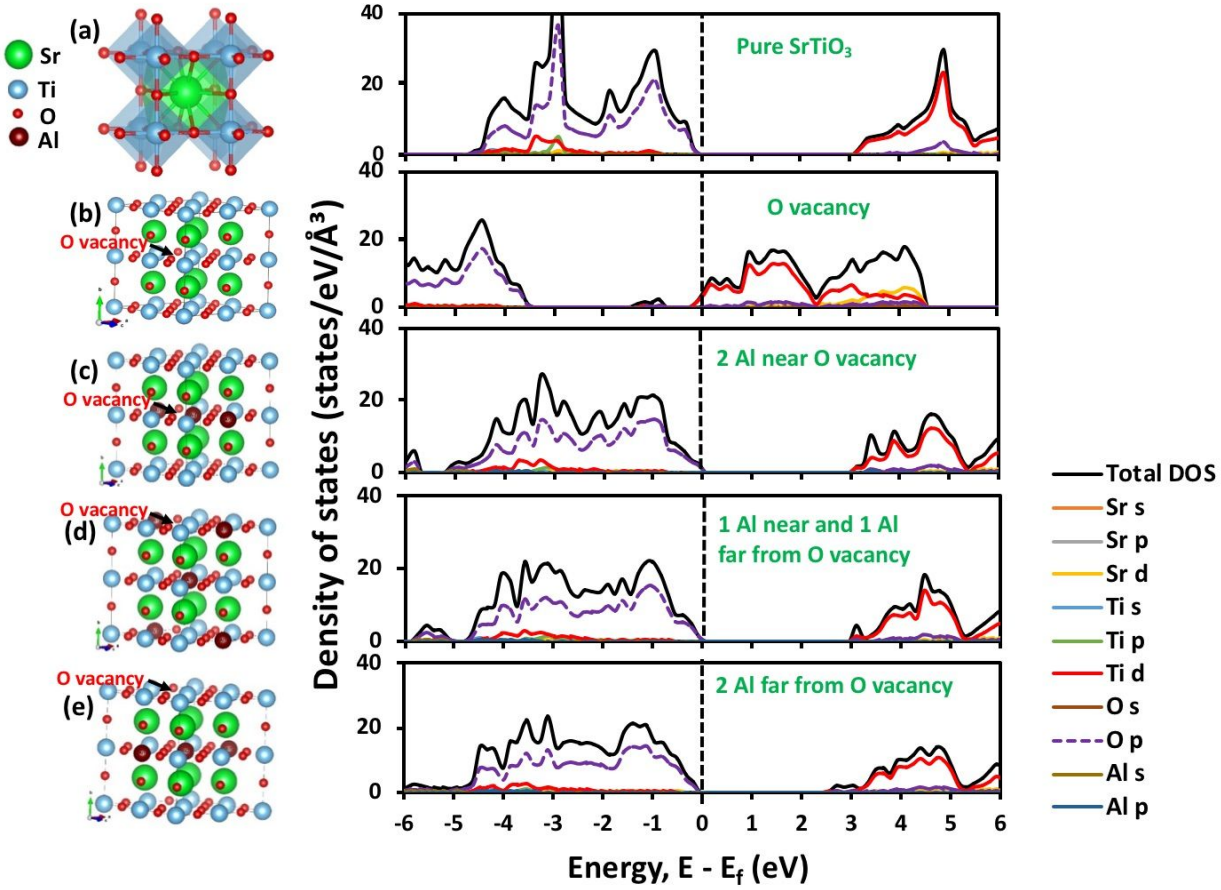

Figure 3. GGA + U projected density of states of (a) pure $SrTiO_3$, (b) $SrTiO_3$ with Vo ($Sr_8Ti_8O_{23}$) and (c-e) Al:$SrTiO_3$ with Vo ($Sr_8Ti_6Al_2O_{23}$). For (c), Al^{3+} are close to Vo. For (d), 1 Al^{3+} is close to Vo site while the other is far. For (e), both Al^{3+} are far from Vo. The Fermi level (E_f) is set at 0 eV.

In order to obtain information about the carrier dynamics of Al-doped $SrTiO_3$, we employ surface photovoltage spectroscopy (SPS) as a sensitive probe of photochemical charge separation. [23, 72-74] In SPS, the surface potential change of an illuminated sample film is monitored with a vibrating Kelvin probe. [75, 76] SPS data for $SrTiO_3$ and Al:$SrTiO_3$ particle films on Au or FTO

substrates are shown in **Figure 4a, b** and **c**. Both samples produce negative photovoltage in agreement with electron movement toward the FTO support and n-type character. The effective bandgap can be approximated from a tangential fit of the major photovoltage feature. [77] This yields 3.0 eV for $SrTiO_3$ and 2.9 eV for Al doped $SrTiO_3$, slightly below the optical band gap. The sub-band gap photovoltage in the 2.0-3.0 eV interval is attributed to excitation of surface defects in both samples.[76] Both compounds reach their maximum photovoltage at 3.4-3.5 eV, just above the optical absorption edge. The voltage is also film thickness-dependent and reaches –3.3 V for a 6.5 μm thick Al:$SrTiO_3$ particle film (**Figure 4c**). This optimum thickness agrees well with the optical absorption depth $2/\alpha$ of the material at 3.4 eV (**Figure 1g**). For films thinner than $2/\alpha$, light absorption limits the photovoltage, while for films thicker than $2/\alpha$, electron transport to the FTO limits the voltage. The data suggests that the electron diffusion length is enhanced in Al:$SrTiO_3$ over that in the non-doped material, for which the photovoltage maximum is lower (–2.4 V) and occurs for a thinner film (2.6 μm). Interestingly, for the thinnest Al:$SrTiO_3$ films a small positive photovoltage is seen also (**Figure 4b**). This signal inversion is attributed to the formation of a space charge layer at the Al:$SrTiO_3$/Au interface, similar to CdSe particle films [78] or for polyhexylthiophene films. [79] The fact that this feature only occurs in the Al:$SrTiO_3$ film suggests that the space charge width is increased as expected from the lower free electron density (Ti^{3+} content).

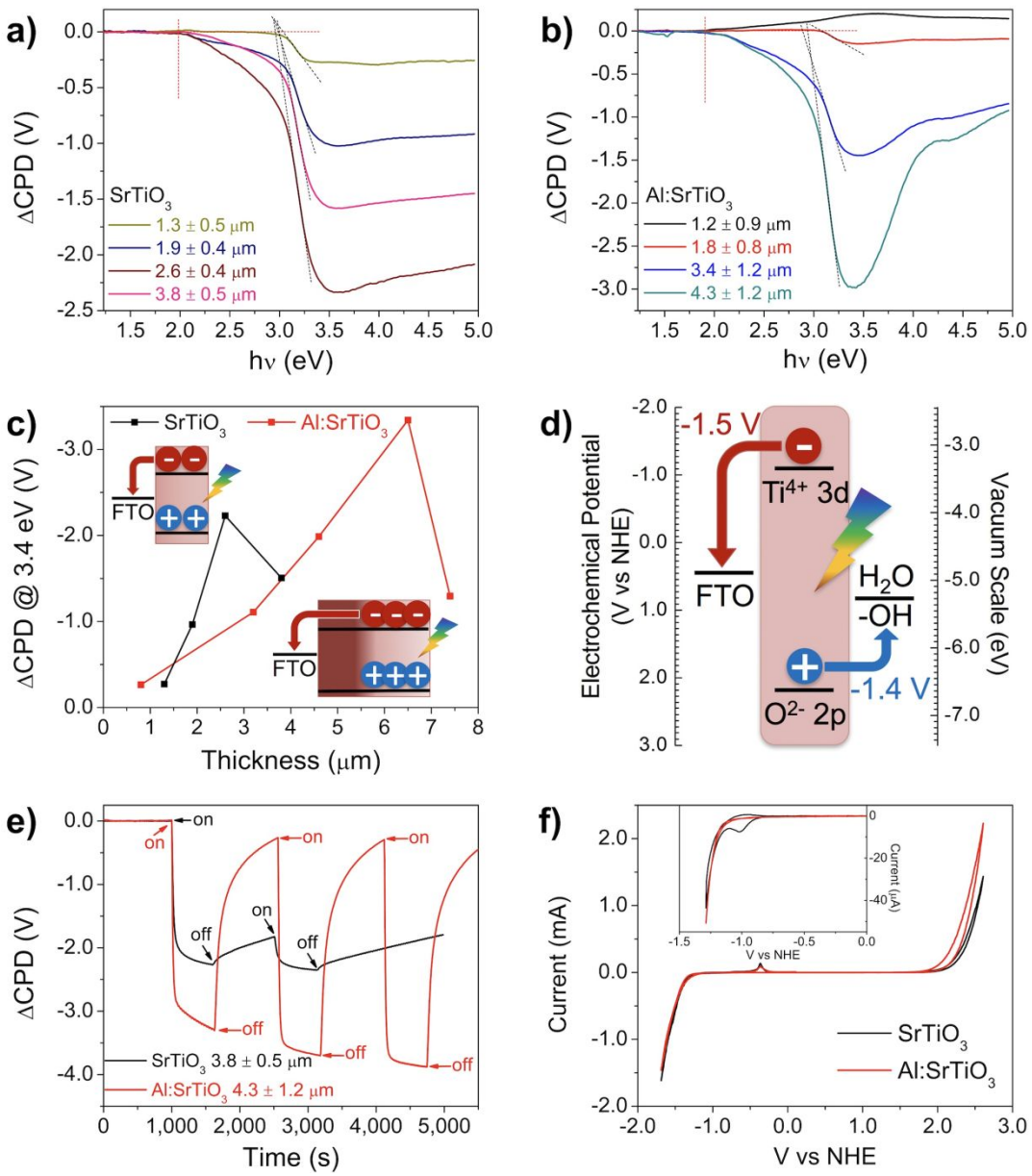

Figure 4. Surface photovoltage spectra of (a) $SrTiO_3$ and (b) Al:$SrTiO_3$ on Au substrate with different thickness. (c) Thickness dependence of maximum photovoltage at 3.4 eV for $SrTiO_3$ and Al:$SrTiO_3$. (d) Energy diagram for $SrTiO_3$ on FTO during SPS measurement. (e) Transient photovoltage with temporary 3.4 eV illumination for $SrTiO_3$ and Al:$SrTiO_3$ films on Au substrate. (f) Cyclic voltammetry scans for non-illuminated $SrTiO_3$ and Al:$SrTiO_3$ films in 0.1 M aqueous K_2SO_4 (insert: cathodic scan from 0 V to -1.3 V and back).

Based on the energy diagram in **Figure 4d** photovoltage generation in Al-doped $SrTiO_3$ involves two separate charge carrier transfer processes. One is electron injection from the conduction band of $SrTiO_3$ into the FTO substrate and the second is hole injection from the Al:$SrTiO_3$ valence band into surface states. Combination of both processes enables a theoretical photovoltage of -1.5 V + (–1.4 V) = –2.9 V. The larger experimental value of –3.3 V for Al:$SrTiO_3$ suggests the presence of an additional photovoltage generating component, likely linked to the oxidation of trace organic impurities at the crystal surface. In combination with strongly reducing species, surface photovoltage values exceeding the band gap of the absorbers are frequently observed. [23] **Figure 4e** also shows transient photovoltage experiments with 3.4 eV illumination. Photovoltage generation for Al:$SrTiO_3$ is nearly fully reversible on the 15 min timescale, while photovoltage generation for $SrTiO_3$ is only 20% reversible, on the basis of the residual voltage after 30 mins. The residual photovoltage for $SrTiO_3$ is attributed to hole trapping at Ti^{3+} sites in the $SrTiO_3$ lattice and at the surface. The much lower residual photovoltage for Al:$SrTiO_3$ agrees with the reduction of hole trapping states (likely Ti^{3+}) in the material.

Electrochemical measurements on non-illuminated $SrTiO_3$ and Al:$SrTiO_3$ particle films immersed in 0.1 M aqueous K_2SO_4 electrolyte are shown in **Figure 4f**. Anodic currents above +2.0 V and below -1.5 V are assigned to the oxidation and reduction of water respectively. The oxidative small peak at -0.4 V is assigned to oxidation of titanium hydrides formed at -1.5 V. [80] Additionally, $SrTiO_3$ shows a reductive peak at -1.0 V (see magnified plot in insert) which is assigned to the reduction of surface Ti^{4+} states. The absence of this peak in Al:$SrTiO_3$ further indicates that Al^{3+} doping in Al:$SrTiO_3$ reduces the formation of Ti^{3+} under cathodic bias. Additionally, the anodic current onset for Al:$SrTiO_3$ is shifted approximately 0.2 V towards less

oxidizing potential. This suggests that hole transport is improved in Al:$SrTiO_3$, which would agree with the lower n-type character as observed in the XPS data in **Figure 2** and as predicted by **Equation 4**.

Figure 5 summarizes the energy diagrams of non-doped $SrTiO_3$ and Al-doped $SrTiO_3$ under illumination. Before Al^{3+} incorporation, each oxygen vacancy in $SrTiO_3$ is associated with two Ti^{3+} states 0.8-1.3 eV below the conduction band. The Ti^{3+} ions are deep electron traps that promote rapid Shockley Read Hall recombination with the photoholes. [81, 82] This reduces the steady state hole concentration under illumination and with it the driving force for OWS. The introduction of Al^{3+} eliminates the Ti^{3+} recombination states, which enables prolonged lifetimes of photoholes and electrons, as observed in transient IR spectra. [29] This improves the photovoltage of the compound and promotes the water splitting reaction. The DFT results show that complete elimination of sub-bandgap states occurs only when the Al^{3+} ions are close to the oxygen vacancies in the compound.

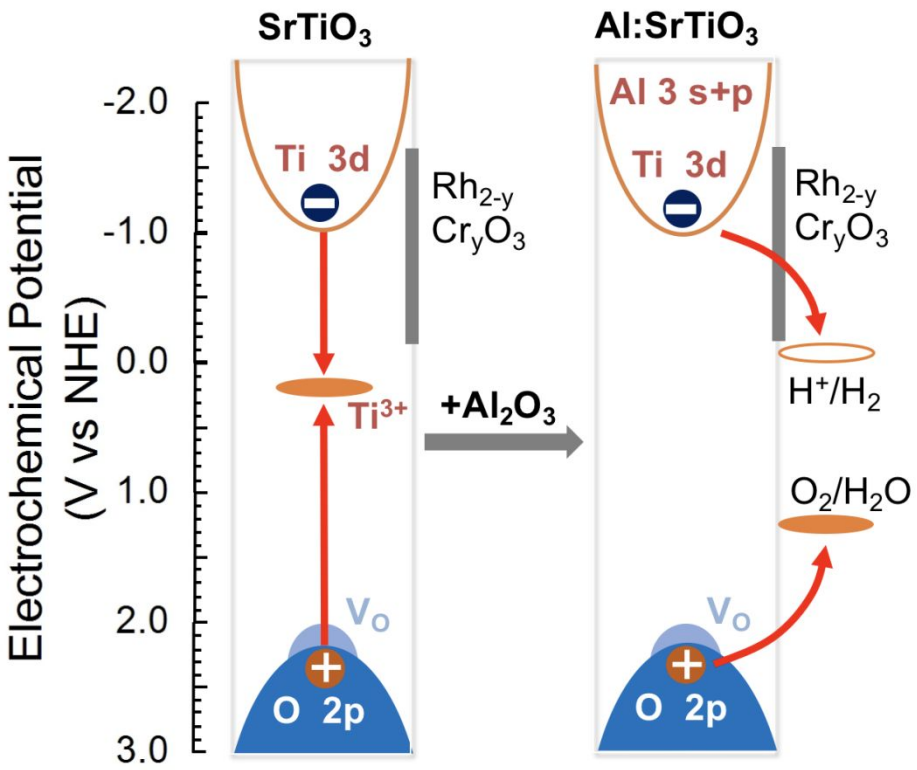

Figure 5. Schematic energy diagrams for $SrTiO_3$ and Al:$SrTiO_3$, illustrating the effect of Al^{3+} on Ti^{3+} sites and on electron/hole recombination.

When the Al^{3+} ions are more than a few atoms away from the V_O center, new Ti^{4+} states approximately 0.5-1.0 eV below the conduction band appear in Al:$SrTiO_3$. Theoretically, these Ti^{4+} states are expected to trap electrons and holes and diminish the photocatalytic activity of $SrTiO_3$. However, this is not observed in the water splitting tests or in the electrochemical or surface photovoltage experiments. One reason is that the Ti^{4+} sites are further away from the mid-band gap position than the Ti^{3+} sites in non-doped $SrTiO_3$ (see **Figure 3**). States close to the mid-band gap position are most detrimental to recombination because they are equally accessible to electrons and holes. Secondly, the incorporation of Al^{3+} reduces the free electron concentration in Al-doped $SrTiO_3$, evident from the 0.5 eV Fermi energy shift seen in the XPS and VB-XPS data.

The combination of the E_F anodic shift of 0.5 eV with the Ti^{4+} cathodic shift of ~0.3 eV reduces the electron population n_t in the Ti^{4+} sub-band gap states by 14 orders of magnitude (at room temperature) based on equation 5. [81, 82]

$$n_T = N_T exp\left(-\frac{E_T - E_F}{kT}\right) \qquad \text{Eq. 5}$$

Here, n_T is the electron population of the trap states, N_T is the density of trap states, E_T is the trap state energy, and E_F is the Fermi level. This reveals that a significant improvement of the photocatalytic activity of Al-doped $SrTiO_3$ can be attributed to the reduced n-character of the compound. This reduced n-type character also widens the depletion layer of the material, as evident in the surface photovoltage spectrum, and as demonstrated recently for Mg-doped $SrTiO_3$, [26] thus improving minority carrier extraction from the compound.

CONCLUSION

In summary, we use X-ray photoelectron spectroscopy and density functional theory results to understand the mechanism by which aliovalent doping of Al^{3+} into $SrTiO_3$ increases the OWS activity of the material. Incorporation of Al^{3+} into the lattice not only eliminates deep Ti^{3+} recombination sites, as previously suggested by Takata et al., [27] but also lowers the Fermi level by approximately 0.5 eV, making the compound less n-type. The detailed effect of Al^{3+} depends sensitively on the relative location to the oxygen vacancies. If the V_O site is surrounded by fewer than two Al^{3+} ions, shallow Ti^{4+} acceptor states are formed near the vacancy. These $\{Ti^{4+}\text{-}V_O\}$ vacancy complexes are responsible for the weak optical absorption of $Al{:}SrTiO_3$, which gives rise

to its pale-brown color. However, because of the lower Fermi level, these Ti^{4+} states are not permanently populated by electrons and thus only mildly promote electron-hole recombination. This is confirmed by the enhanced reversibility of the surface photovoltage and by electrochemical scans. These changes explain the vastly improved overall water splitting activity of aliovalent doped $SrTiO_3$, as observed here and by the Domen group. [27, 31, 35] Separately, our work also provides the first example of a type 1 single bed particle suspension 'baggie' reactor for overall water splitting under natural sunlight illumination. With Al-doped $SrTiO_3/Rh_{2-y}Cr_yO_3$ as a photocatalyst the device achieves a solar to hydrogen efficiency (STH) of 0.11%. This experimentally verifies one of the model assumptions of the 2009 US Department of Energy technoeconomic analysis for photoelectrochemical hydrogen production. With its 3.2 eV band gap, the solar to hydrogen STH efficiency of $SrTiO_3$ is fundamentally limited to 2.5%, but values of up to 14.4% STH are theoretically possible by using metal oxides with band gaps near the 2.0 - 2.5 eV optimum for a single absorber, if ways can be found to overcome the carrier lifetime limitations of these materials. [83-87] The results of this work suggest that aliovalent doping may be a one way to achieve this goal with metal oxides.

Supporting Information

SEM images and powder X-ray diffraction patterns, irradiance data and gas evolution data, optical spectra, XPS spectra, DFT calculated band structures, and a movie showing gas evolution from a catalyst suspension in direct sunlight.

Conflicts of Interest

There are no conflicts of interest to declare.

ACKNOWLEDGMENT

FEO thanks the National Science Foundation for financial support through grant CHE 1464938. Surface photovoltage measurements were performed with funding from the U.S. Department of Energy, Office of Science, Basic Energy Sciences under Award # DE-SC0015329. RVG would like to thank the support by São Paulo Research Foundation (FAPESP - 15/23503-3) and MNH acknowledges the support by National Science Foundation award no. SusChEM 1609811. All computations were done at Texas Advance Computing Center (TACC) in Austin. A.J.M. acknowledges support from the University of California Advanced Solar Technologies Institute/UC Solar (UC Office of the President MRPI #328386).

Notes

a Department of Chemistry, University of California, Davis. One Shields Avenue, Davis, CA, 95616, USA. Fax: (+1) 530 752 8995; E-mail: fosterloh@ucdavis.edu

b São Carlos Institute of Physics, University of São Paulo, PO Box 369, 13560-970 São Carlos, SP, Brazil

c Department of Physics, The University of Texas at Arlington, Texas, 76019, USA

d Department of Chemical Engineering, University of California, Davis. One Shields Avenue, Davis, CA, 95616, USA

REFERENCES

1. F. E. Osterloh, in *Integrated Solar Fuel Generators*, The Royal Society of Chemistry, 2019, DOI: 10.1039/9781788010313-00214, pp. 214-280.
2. B. A. Pinaud, J. D. Benck, L. C. Seitz, A. J. Forman, Z. B. Chen, T. G. Deutsch, B. D. James, K. N. Baum, G. N. Baum, S. Ardo, H. L. Wang, E. Miller and T. F. Jaramillo, *Energ. Environ. Sci.*, 2013, **6**, 1983-2002.
3. B. D. James, G. N. Baum, J. Perez and K. N. Baum, http://www1.eere.energy.gov/hydrogenandfuelcells/pdfs/pec_technoeconomic_analysis.pdf).
4. A. Kudo and Y. Miseki, *Chem. Soc. Rev.*, 2009, **38**, 253-278.
5. K. Sivula and R. van de Krol, *Nature Reviews Materials*, 2016, **1**, 15010.
6. D. M. Fabian, S. Hu, N. Singh, F. A. Houle, T. Hisatomi, K. Domen, F. E. Osterloh and S. Ardo, *Energ. & Envi. Sci.*, 2015, **8**, 2825-2850.
7. K. Maeda, K. Teramura and K. Domen, *J. Catal.*, 2008, **254**, 198-204.
8. Q. Wang, T. Hisatomi, Q. Jia, H. Tokudome, M. Zhong, C. Wang, Z. Pan, T. Takata, M. Nakabayashi, N. Shibata, Y. Li, I. D. Sharp, A. Kudo, T. Yamada and K. Domen, *Nat. Mater.*, 2016, **15**, 611–615.
9. Q. Wang, T. Hisatomi, Y. Suzuki, Z. Pan, J. Seo, M. Katayama, T. Minegishi, H. Nishiyama, T. Takata, K. Seki, A. Kudo, T. Yamada and K. Domen, *J. Am. Chem. Soc.*, 2017, **139**, 1675-1683.

10. R. Sathre, C. D. Scown, W. R. Morrow, J. C. Stevens, I. D. Sharp, J. W. Ager, K. Walczak, F. A. Houle and J. B. Greenblatt, *Energ. & Environ. Sci.*, 2014, DOI: 10.1039/C4EE01019A.

11. T. Ohno, L. Bai, T. Hisatomi, K. Maeda and K. Domen, *J. Am. Chem. Soc.*, 2012, **134**, 8254-8259.

12. H. Kato, K. Asakura and A. Kudo, *J. Am. Chem. Soc.*, 2003, **125**, 3082-3089.

13. Y. Sakata, T. Hayashi, R. Yasunaga, N. Yanaga and H. Imamura, *Chem. Commun.*, 2015, **51**, 12935-12938.

14. F. E. Osterloh, *Chem. Mater.*, 2008, **20**, 35-54.

15. C. X. Kronawitter, L. Vayssieres, S. H. Shen, L. J. Guo, D. A. Wheeler, J. Z. Zhang, B. R. Antoun and S. S. Mao, *Energ. & Environ. Sci.*, 2011, **4**, 3889-3899.

16. M. S. Wrighton, A. B. Ellis, P. T. Wolczanski, D. L. Morse, H. B. Abrahamson and D. S. Ginley, *J. Am. Chem. Soc.*, 1976, **98**, 2774-2779.

17. J. G. Mavroides, J. A. Kafalas and D. F. Kolesar, *Appl. Phys. Lett.*, 1976, **28**, 241-243.

18. A. Kumar, P. G. Santangelo and N. S. Lewis, *J. Phys. Chem.*, 1992, **96**, 834-842.

19. K. Domen, A. Kudo, T. Onishi, N. Kosugi and H. Kuroda, *J. Phys. Chem. C.*, 1986, **90**, 292-295.

20. K. Domen, S. Naito, M. Soma, T. Onishi and K. Tamaru, *J. Chem. Soc., Chem. Commun.*, 1980, 543-544.

21. T. K. Townsend, N. D. Browning and F. E. Osterloh, *ACS Nano*, 2012, **6**, 7420–7426.

22. T. K. Townsend, N. D. Browning and F. E. Osterloh, *Energ & Env. Sci.*, 2012, **5**, 9543-9550.

23. J. Wang, J. Zhao and F. E. Osterloh, *Energ. & Envi. Sci.*, 2015, **8**, 2970-2976.

24. L. Mu, Y. Zhao, A. Li, S. Wang, Z. Wang, J. Yang, Y. Wang, T. Liu, R. Chen, J. Zhu, F. Fan, R. Li and C. Li, *Energ. & Environ. Sci.*, 2016, **9**, 2463-2469.

25. K. Han, T. Kreuger, B. Mei and G. Mul, *ACS Catalysis*, 2017, **7**, 1610-1614.

26. K. Han, Y.-C. Lin, C.-M. Yang, R. Jong, G. Mul and B. Mei, *ChemSusChem*, 2017, **10**, 4510-4516.

27. T. Takata and K. Domen, *J. Phys. Chem. C*, 2009, **113**, 19386-19388.

28. H. Kato, M. Kobayashi, M. Hara and M. Kakihana, *Catalysis Science & Technology*, 2013, **3**, 1733-1738.

29. A. Yamakata, H. Yeilin, M. Kawaguchi, T. Hisatomi, J. Kubota, Y. Sakata and K. Domen, *J. Photoch. Photobio. A*, 2015, **313**, 168-175.

30. Y. Sakata, Y. Miyoshi, T. Maeda, K. Ishikiriyama, Y. Yamazaki, H. Imamura, Y. Ham, T. Hisatomi, J. Kubota, A. Yamakata and K. Domen, *Applied Catalysis A: General*, 2016, **521**, 227-232.

31. Y. Ham, T. Hisatomi, Y. Goto, Y. Moriya, Y. Sakata, A. Yamakata, J. Kubota and K. Domen, *J. Mater. Chem. A*, 2016, **4**, 3027-3033.

32. Y. Sakata, Y. Miyoshi, T. Maeda, K. Ishikiriyama, Y. Yamazaki, H. Imamura, Y. Ham, T. Hisatomi, J. Kubota, A. Yamakata and K. Domen, *Applied Catalysis A: General*, 2016, **521**, 227-232.

33. K. Maeda, K. Teramura, D. L. Lu, T. Takata, N. Saito, Y. Inoue and K. Domen, *Nature*, 2006, **440**, 295-295.

34. K. Maeda, K. Teramura, D. L. Lu, N. Saito, Y. Inoue and K. Domen, *J. Phys. Chem. C*, 2007, **111**, 7554-7560.

35. Y. Goto, T. Hisatomi, Q. Wang, T. Higashi, K. Ishikiriyama, T. Maeda, Y. Sakata, S. Okunaka, H. Tokudome, M. Katayama, S. Akiyama, H. Nishiyama, Y. Inoue, T. Takewaki, T. Setoyama, T. Minegishi, T. Takata, T. Yamada and K. Domen, *Joule*, 2018, **2**, 509-520.

36. H. Lyu, T. Hisatomi, Y. Goto, M. Yoshida, T. Higashi, M. Katayama, T. Takata, T. Minegishi, H. Nishiyama, T. Yamada, Y. Sakata, K. Asakura and K. Domen, *Chemical Science*, 2019, DOI: 10.1039/C8SC05757E.

37. Z. Zhao, E. J. Willard, H. Li, Z. Wu, R. H. R. Castro and F. E. Osterloh, *Journal of Materials Chemistry A*, 2018, **6**, 16170-16176.

38. K. Maeda, K. Teramura, D. Lu, T. Takata, N. Saito, Y. Inoue and K. Domen, *Nature*, 2006, **440**, 295.

39. K. Maeda, K. Teramura, N. Saito, Y. Inoue and K. Domen, *Journal of Catalysis*, 2006, **243**, 303-308.

40. K. Maeda, K. Teramura, H. Masuda, T. Takata, N. Saito, Y. Inoue and K. Domen, *J. Phys. Chem. B*, 2006, **110**, 13107-13112.

41. P. Hohenberg and W. Kohn, *Physical Review*, 1964, **136**, B864-B871.

42. W. Kohn and L. J. Sham, *Physical Review*, 1965, **140**, A1133-A1138.

43. G. Kresse and J. Furthmüller, *Physical Review B*, 1996, **54**, 11169-11186.

44. G. Kresse and J. Furthmüller, *Computational Materials Science*, 1996, **6**, 15-50.

45. P. E. Blöchl, *Physical Review B*, 1994, **50**, 17953-17979.

46. M. Gajdoš, K. Hummer, G. Kresse, J. Furthmüller and F. Bechstedt, *Physical Review B*, 2006, **73**, 045112.

47. J. P. Perdew, K. Burke and Y. Wang, *Physical Review B*, 1996, **54**, 16533-16539.

48. J. D. Pack and H. J. Monkhorst, *Physical Review B*, 1977, **16**, 1748-1749.

49. S. L. Dudarev, G. A. Botton, S. Y. Savrasov, C. J. Humphreys and A. P. Sutton, *Physical Review B*, 1998, **57**, 1505-1509.

50. R. P. Vasquez, *Surf. Sci. Spectra*, 1992, **1**, 129-135.

51. S. Ferrer and G. A. Somorjai, *Surf. Sci.*, 1980, **94**, 41-56.

52. H. Tan, Z. Zhao, W.-b. Zhu, E. N. Coker, B. Li, M. Zheng, W. Yu, H. Fan and Z. Sun, *ACS Appl. Mater. Interfaces*, 2014, **6**, 19184-19190.

53. Y. Fu, H. Du, S. Zhang and W. Huang, *Materials Science and Engineering: A*, 2005, **403**, 25-31.

54. P. V. Nagarkar, P. C. Searson and F. D. G. III, *J. Appl. Phys.*, 1991, **69**, 459-462.

55. J. F. Moulder and J. Chastain, *Handbook of X-ray Photoelectron Spectroscopy: A Reference Book of Standard Spectra for Identification and Interpretation of XPS Data*, Physical Electronics Division, Perkin-Elmer Corporation, 1992.

56. Y. Zhu, P. A. Salvador and G. S. Rohrer, *Chem. Mater.*, 2016, **28**, 5155-5162.

57. E. McCafferty and J. P. Wightman, *Surf. Interface Anal.*, 1998, **26**, 549-564.

58. M. E. Kazzi, G. Delhaye, C. Merckling, E. Bergignat, Y. Robach, G. Grenet and G. Hollinger, *Journal of Vacuum Science & Technology A*, 2007, **25**, 1505-1511.

59. T. Sun and M. Lu, *Appl. Phys. A*, 2012, **108**, 171-175.

60. M. Copel, P. R. Duncombe, D. A. Neumayer, T. M. Shaw and R. M. Tromp, *Appl. Phys. Lett.*, 1997, **70**, 3227-3229.

61. Q. Fu and T. Wagner, *Surf. Sci. Rep.*, 2007, **62**, 431-498.

62. F. A. Kröger and H. J. Vink, in *Solid State Physics*, eds. F. Seitz and D. Turnbull, Academic Press, 1956, vol. 3, pp. 307-435.

63. R. Krol, *Photoelectrochemical Hydrogen Production*, 2012, **102**, 13-67.

64. G. Perluzzo and J. Destry, *Can. J. Phys.*, 1978, **56**, 453-467.

65. J. L. G. Fierro, *Metal oxides : chemistry and applications*, CRC Taylor & Francis, Boca Raton, FL, 2006.

66. R. A. Rosenberg, Y. Choi, K. Vijayalakshmi, M. Kareev, J. Tchakhalian, S. Balaz and L. J. Brillson, *Appl. Phys. Lett.*, 2013, **102**, 192910.

67. S. Piskunov, E. Heifets, R. I. Eglitis and G. Borstel, *Computational Materials Science*, 2004, **29**, 165-178.

68. H. Salehi, *Journal of Modern Physics*, 2011, **2**, 934-943.

69. K. v. Benthem, C. Elsasser and R. H. French, *J. Appl. Phys.*, 2001, **90**, 6156-6164.

70. J. Zhang, S. Walsh, C. Brooks, D. G. Schlom and L. J. Brillson, *Journal of Vacuum Science & Technology B: Microelectronics and Nanometer Structures Processing, Measurement, and Phenomena*, 2008, **26**, 1466-1471.

71. Y. Lei, L. D. Zhang, G. W. Meng, G. H. Li, X. Y. Zhang, C. H. Liang, W. Chen and S. X. Wang, *Appl. Phys. Lett.*, 2001, **78**, 1125-1127.

72. J. Zhao and F. E. Osterloh, *J. Phys. Chem. Lett*, 2014, **5**, 782–786.

73. M. Kodera, J. Wang, B. A. Nail, J. Liu, H. Urabe, T. Hisatomi, M. Katayama, T. Minegishi, F. E. Osterloh and K. Domen, *Chem. Phys. Lett.*, 2017, **683**, 140-144.

74. M. A. Melo, Z. Wu, B. A. Nail, A. T. De Denko, A. F. Nogueira and F. E. Osterloh, *Nano Lett.*, 2018, **18**, 805-810.

75. L. Kronik and Y. Shapira, *Surf. Sci. Rep.*, 1999, **37**, 1-206.

76. H. C. Gatos and J. Lagowski, *J. Vac. Sci. Technol.*, 1973, **10**, 130-135.

77. D. Gal, Y. Mastai, G. Hodes and L. Kronik, *J. Appl. Phys.*, 1999, **86**, 5573-5577.

78. J. Zhao, B. A. Nail, M. A. Holmes and F. E. Osterloh, *The Journal of Physical Chemistry Letters*, 2016, **7**, 3335-3340.

79. F. E. Osterloh, M. A. Holmes, L. Chang, A. J. Moule and J. Zhao, *J.Phys.Chem. C*, 2013, **117**, 26905–26913.

80. R. M. Torresi, O. R. Cámara and C. P. De Pauli, *Electrochim. Acta*, 1987, **32**, 1357-1363.

81. S. M. Sze, *Semiconductor devices, physics and technology*, Wiley, New York, 2nd edn., 2002.

82. T. Dittrich, *Materials concepts for solar cells*, Imperial College Press, London, 2015.

83. J. R. Bolton, S. J. Strickler and J. S. Connolly, *Nature*, 1985, **316**, 495-500.

84. R. E. Rocheleau and E. L. Miller, *Int. J. Hydrogen Energ.*, 1997, **22**, 771-782.

85. O. K. Varghese and C. A. Grimes, *Sol. Energ. Mat. Sol. C*, 2008, **92**, 374-384.

86. L. C. Seitz, Z. Chen, A. J. Forman, B. A. Pinaud, J. D. Benck and T. F. Jaramillo, *ChemSusChem*, 2014, **7**, 1372-1385.

87. K. T. Fountaine, H. J. Lewerenz and H. A. Atwater, *Nat. Commun.*, 2016, **7**, 13706.

Broader context

Water electrolysis provides a pathway to hydrogen as a clean, non-carbon emitting fuel. When coupled to photovoltaic or photoelectrochemical cells, the process can be used to store photovoltaic energy from the sun, thereby creating the basis for a sustainable solar fuel cycle. According to a recent technoeconomic analysis conducted by the U.S. Department of Energy, photocatalysts may be most cost effective and most scalable technology for the water splitting reaction. The problem is that none of the known photocatalysts yet reach their theoretical energy conversion efficiency limit of 14.4%. This is because solar energy conversion with small particles is limited by slow carrier transport, insufficient carrier separation, and fast recombination at the particle surfaces. As Goto et al. showed (*Joule* **2018,** *2* (3), 509-520), introduction of approximately 1% Al ions into $SrTiO_3$ can boost the solar to hydrogen conversion efficiency of this material to 0.4 %. Here we report the underlying mechanism of the enhancement. Our findings suggest that aliovalent doping may be a general method to improve the photocatalytic properties of metal oxides. We also demonstrate overall water splitting with a type 1 single bed particle suspension 'baggie' reactor under direct sunlight illumination for the first time.